Contrib Mineral Petrol (1996) 123: 345–357

D. L. Kohlstedt · H. Keppler · D. C. Rubie

Solubility of water in the α, β and γ phases of $(Mg,Fe)_2SiO_4$

Received: 10 February 1995 / Accepted: 23 October 1995

Abstract The solubility of hydroxyl in the α, β and γ phases of $(Mg,Fe)_2SiO_4$ was investigated by hydrothermally annealing single crystals of San Carlos olivine. Experiments were performed at a temperature of 1000° or 1100 °C under a confining pressure of 2.5 to 19.5 GPa in a multianvil apparatus with the oxygen fugacity buffered by the Ni:NiO solid-state reaction. Hydroxyl solubilities were determined from infrared spectra obtained of polished thin sections in crack-free regions ≤100 μm in diameter. In the α-stability field, hydroxyl solubility increases systematically with increasing confining pressure, reaching a value of ~20,000 H/10^6Si (1200 wt ppm H_2O) at the α-β phase boundary near 13 GPa and 1100 °C. In the β field, the hydroxyl content is ~400,000 H/10^6Si (24,000 wt ppm H_2O) at 14–15 GPa and 1100 °C. In the γ field, the solubility is ~450,000 H/10^6Si (27,000 wt ppm H_2O) at 19.5 GPa and 1100 °C. The observed dependence of hydroxyl solubility with increasing confining pressure in the α phase reflects an increase in water fugacity with increasing pressure moderated by a molar volume term associated with the incorporation of hydroxyl ions into the olivine structure. Combined with published results on the dependence of hydroxyl solubility on water fugacity, the present results for the α phase can be summarized by the relation $C_{OH} = A(T) f_{H_2O}^{n} \exp(-P\Delta V/RT)$, where $A(T)$ = 1.1 H/10^6Si/MPa at 1100 °C, n = 1, and $\Delta V = 10.6\times10^{-6}$ m^3/mol. These data demonstrate that the entire present-day water content of the upper mantle could be incorporated in the mineral olivine alone; therefore, a free hydrous fluid phase cannot be stable in those regions of the upper mantle with a normal concentration of hydrogen. Free hydrous fluids are restricted to special tectonic environments, such as the mantle wedge above a subduction zone.

D. L. Kohlstedt (✉)[1]· H. Keppler · D. C. Rubie
Bayerisches Geoinstitut, Universität Bayreuth,
D-94550 Bayreuth, Germany

[1]*Present address:*
On sabbatical leave from Department of Geology and Geophysics, Pillsbury Hall, University of Minnesota, Minneapolis, MN 55455, USA

Editorial responsibility: T.L. Grove

Introduction

The water contents in the main reservoirs of the upper mantle are estimated to range from 100 to 500 ppm by weight of H_2O for the depleted, undepleted and enriched source regions of various types of magmas (Bell and Rossman 1992). These estimates are based on two lines of reasoning. First, measurements of the water contents of quenched basaltic glasses can be combined with the partition coefficients of hydrogen and the inferred degree of partial melting of the source region to reconstruct the original water content in the mantle source. Second, measurements of water contents of mantle xenoliths can be used to estimate the water contents of the upper mantle, provided that no loss of hydrogen occurred upon decompression. Both methods yield similar values, on the order of a few hundred ppm by weight of H_2O for most accessible mantle reservoirs. However, investigation of natural samples cannot determine whether these amounts of water are sufficient to form a free hydrous fluid phase in the mantle, can be accommodated in nominally anhydrous minerals, or require the presence of special hydrous phases. To answer these questions, experimental calibration of the equilibrium solubility of water in nominally anhydrous minerals coexisting with a hydrous fluid phase is necessary. Until now, such calibrations were not available for the pressure and temperature conditions of the upper mantle. Bai and Kohlstedt (1992, 1993) reported the results of solubility experiments with olivine up to 300 MPa. Young et al. (1993) showed that substantial amounts of OH can be incorporated in the α and β phases at mantle pressures. However, their experiments did not include a free hydrous fluid phase; as a result, their data only provide lower limits for the equilibrium solubility.

Even a small amount of water substantial influences the physical properties of silicate rocks. If a few hundred ppm of water-derived species are present, the high-temperature creep strength of olivine single crystals and olivine-rich rocks decreases by a factor of 2 to 3 (Carter and Ave'Lallemant 1970; Blacic 1972; Chopra and Paterson 1984; Mackwell et al. 1985; Karato et al. 1986). Hydrogen ions introduced into the olivine structure in the presence of water may also markedly enhance the electrical conductivity of olivine (Karato 1990). In addition, point defects generated on the silicon, oxygen and metal sublattices when hydrogen or hydroxyl are incorporated into the olivine structure should influence significantly the ionic diffusivities and related kinetic properties.

To determine the importance of nominally anhydrous minerals as reservoirs for water in the mantle and to understand the influence of water on their physical properties, quantification of the solubility of water-derived species in the olivine structure is necessary. Previous experiments at pressures between 50 and 300 MPa demonstrate that the hydroxyl concentration determined from infrared spectra increases systematically with increasing water fugacity (Bai and Kohlstedt 1992). However, extrapolation of these results to much higher pressures appropriate to the upper mantle requires not only understanding the effect of water fugacity on solubility but also determination of the influence of pressure on solubility. Hence, in the present study, the dependence of hydroxyl concentration as a function of pressure and water fugacity in the α-stability field was measured for samples hydrothermal annealed under water-saturated conditions in a multianvil apparatus. In addition, hydrothermal experiments were carried out in the β- and γ-stability fields to determine the solubility in all three polymorphs of $(Mg,Fe)_2SiO_4$.

Experimental procedure

Samples and encapsulation

All but one of the samples used in the high-pressure, high-temperature annealing experiments were prepared from an oriented single crystal of olivine from San Carlos, Arizona, of approximate composition $(Mg_{0.90}Fe_{0.10})_2SiO_4$. For the first of the two experiments in the γ field (sample γ1 in Table 1), the starting sample was a powder consisting of 95% olivine plus 5% orthopyroxene with a grain size of $\sim$25 μm. The single-crystal samples were cut into rectangular parallelpipeds of dimensions 0.7×0.8×0.9 mm with surfaces parallel to the (100), (010) and (001) crystallographic planes, respectively. The surfaces parallel to (010) were polished, so that they could be easily identified when a sample was loaded into a capsule.

For experiments in the α-stability field, capsules were fabricated from Pt tube with an outer diameter of 2.0 mm and a wall thickness of 0.1 mm. After one end was welded shut and flattened, the bottom of the capsule was covered with two discs of Ni foil and the inner cylindrical surface was lined with a single layer of 0.1-mm thick Ni foil; the nickel was included to buffer the oxygen fugacity by the Ni:NiO reaction. A mixture of talc plus brucite powder in the ratio 1.4:1 by weight was then packed into the bottom half of the capsule; this ratio yields water plus approximately a 9:1 ratio of olivine to enstatite after dehydration and reaction. A square indentation, approximately 1 mm on a side, was made in the compacted powder with a punch, and a sample was positioned in this space with the [010] direction parallel to the cylindrical axis of the capsule. Additional powder was packed on top of the sample and covered by two discs of Ni foil. Finally, the second end of the capsule was welded shut and flattened to yield a final capsule length of $\sim$3.2 mm, with $\sim$0.4 mm of Pt at each end. In most cases, a pinhole remained after welding, but it appeared to close during flattening of the end and/or pressurization of the sample assembly. For experiments in the β- and γ-stability fields, the capsules were similar, but smaller, in order to fit into the smaller multianvil assemblies required to attain higher pressures. Schematic cross sections of comparable capsule assemblies are published in Rubie et al. (1993a, Fig. 2).

High-pressure annealing experiments

The high-pressure annealing experiments were carried out in a split-sphere multianvil apparatus. Tungsten carbide anvils with truncation edge lengths of 11, 8 and 5 mm were used for experiments at pressures of 2.5 to 10.0 GPa, 12.0 to 15.0 GPa and 19.5 GPa, respectively. Octahedral sample assemblies with edge lengths of 18, 14 and 10 mm were fabricated from partially sintered 95% MgO + 5% Cr_2O_3. A zirconia sleeve insulates the cylindrical $LaCrO_3$ heater from the octrahedron; a stepped geometry for the heater reduces temperature gradients in the 18 and 14 mm octahedral sample assemblies (Rubie et al. 1993a). Similarly, a MgO sleeve insulates the sample capsule from the heater. Spacers of MgO position the sample capsule near the middle of the high-pressure assembly; the bottom spacer was solid and the top spacer hollow. A W3%Re-W25%Re thermocouple sheathed in a four-bore Al_2O_3 tube directly contacts the top end of the sample assembly. The pressure was calibrated at high temperature using phase transformations in SiO_2 and Mg_2SiO_4 and is estimated to be accurate to within ±5% (Rubie et al. 1993b; Canil 1994). The temperature gradient in the region of the sample is estimated to be <20 °C/mm in experiments up to 15 GPa and <50 °C/mm at 19.5 GPa (Rubie et al. 1993a,b; Canil 1994). Cross-sectional views of the high-pressure assemblies used in the experiments at 2–10 GPa and at 19.5 GPa are published elsewhere (Rubie et al. 1993a; Canil 1994).

Annealing experiments were performed at pressures between 2.5 and 19.5 GPa. Pressure was increased under computer control over a period of 2 to 4 h, with longer pressurization times corresponding to higher experimental pressures. All but one of the experiments were carried out at 1100 °C; the one exception (α5) was performed at 1000 °C. Except for one of the experiments in the γ-stability field (γ2), the temperature was increased at 50 °C/min after the experimental pressure was reached in order to minimize loss of water from the capsule. At the completion of the hydrothermal annealing cycle, the temperature was decreased at 50 °C/min to room temperature; subsequently, the pressure was dropped to 0.1 MPa over a period of 4 to 8 h. Most of the samples were held at the annealing temperature and pressure for either 10^4 to 10^5 s. Table 1 summarizes the pressure, temperature and duration of each experiment; values for the water fugacity were calculated from the results of Pitzer and Sterner (1994; private communication SM Sterner, 1993).

To maximize the grain size in the second sample annealed in the γ-phase field (sample γ2), pressurization and heating were carried out in two stages. First, the sample was annealed in the β-stability field at 14 GPa and 1100 °C for 2 h. The pressure was then increased to 19.5 GPa while maintaining the temperature at 1100 °C. After an additional 1 h at 19.5 GPa and 1100 °C, the sample was cooled at 50 °C/min to room temperature, after which the pressure was decreased slowly to 0.1 MPa.

After removing a sample capsule from the high-pressure sample assembly, a small hole was filed into the capsule to test for the presence of water. In all but two of the experiments in the α field,

Table 1 Run conditions and resulting water solubilities.

Sample #	Run #	P (GPa)	f_{H_2O} (GPa)	T (°C)	t (s)	H_2O present	C_{OH} (H/10^6Si)	C_{H_2O} (wt ppm H_2O)
α1	13	2.5	2.4×10^1	1100	1×10^4	✔[b]	2,200	135
α2	14	5	7.0×10^2	"	1×10^4	✔	8,060	496
α3	18	6.5	4.2×10^3	"	1×10^5		>4,700[c]	>290
α4	7	8	2.2×10^4	"	1×10^4	✔	14,100	867
α5	8	8	2.2×10^4	1000	2×10^5	✔	14,400	886
α6	17	8	2.2×10^4	1100	1×10^4	✔	14,600	898
α7	15	8	2.2×10^4	"	1×10^5		>8,000	>490
α8	20	9	6.4×10^4	"	1×10^5	✔	16,000	984
α9	10	10	1.8×10^5	"	1×10^4	✔	17,400	1,070
α10	25	12	1.3×10^6	"	1×10^5	✔	24,600	1,510
α11	16	13	3.4×10^6	"	1×10^5	✔	17,800	1,090
β1	12	14	8.7×10^6	"	1×10^4		>354,000	>21,300
β2	11	15	2.2×10^7	"	1×10^4		>386,000	>23,200
β3	9	15	2.2×10^7	"	1×10^4		>402,000	>24,100
γ1	21	19.5	2.4×10^9	"	1×10^4		>32,000	1,970
γ2	26	19.5	2.4×10^9	"	1×10^4		>437,000	>26,200

[a] Quoted values were calculated for water-present conditions (Pitzer and Sterner 1994)
[b] A ✔ indicates that water was present at the end of the experiment
[c] Reported value is a lower limit, as no water was present at the end of the experiment

water and gas bubbled out of the hole; water was not detected in any of the experiments in the β and γ fields (Table 1). If water was not observed, the sample capsule was weighed, vacuum dried at ~230 °C for 24 h and reweighed. Weight loss was not detected for any of the samples.

Microscopy, electron microprobe and x-ray diffraction characterization

The microstructures of the hydrothermally annealed samples were examined by optical and scanning electron microscopy (SEM). Grain size was estimated from optical micrographs taken with transmitted light. Compositions were measured with a JEOL 8900 Superprobe using four wavelength dispersive spectrometers. In most cases, the concentrations of Si, Mg, Fe and Ni were determined, and the oxygen concentration was calculated by difference. In a few cases, oxygen content was also measured.

Reflection-mode, powder X-ray microdiffraction confirmed the presence of either β phase or γ phase. X-ray diffraction patterns were obtained from polished thin sections of each sample using an X-ray beam collimated to a diameter of 0.1 mm.

Infrared analyses

Infrared spectra were measured using a Bruker IFS 120 HR high-resolution Fourier-transform spectrometer. This spectrometer contains a permanently aligned Michelson-type interferometer with an angle of incidence of 30°. For microanalysis of water contents in olivine and its high-pressure polymorphs, the spectrometer was coupled with a Bruker IR microscope containing all-reflecting, Cassegranian optics. Measurements were carried out using a tungsten light source, a CaF_2 beam-splitter and a high-sensitivity, narrow-band MCT detector. Several hundred, in some cases up to two thousand, scans were accumulated for each spectrum. During the measurements, the optics of the spectrometer were evacuated and the microscope was purged with a stream of H_2O- and CO_2-free purified air. This procedure allows detection of water contents in olivine and similar materials at the level of a few ppb. The minimum spot size that can be analyzed is less than 10 μm in diameter. Polarized infrared radiation was generated using a metal-strip polarizer on a KRS-5 substrate. Background corrections of absorbance spectra were carried out by a spline fit of the baseline defined by points outside the OH-stretching region.

Fourier transform infrared (FTIR) spectra were obtained at room temperature on polished sections prepared from the heat-treated samples in regions <100 μm in diameter that were free of cracks and grain boundaries. In order that the infrared beam would not be totally absorbed at particular wavenumbers in the OH-stretching portion of the spectra, samples of the α phase were ground to a thickness of ~100 μm, while samples of the β and γ phases had to be reduced to a thickness of <20 μm. For samples annealed in the olivine stability field, surfaces of the polished thin section were parallel to (010). Both unpolarized and polarized spectra were collected from the oriented olivine samples. Two sets of polarized spectra were collected, one with the electric field vector of the infrared beam parallel to the [100] crystallographic direction and the other with the electric field vector parallel to [001]. Only unpolarized spectra were collected from the unoriented grains of the β and γ phases.

To determine the concentrations of hydroxyl groups in the annealed samples, the infrared spectra were integrated from approximately 3780 to 2950 cm^{-1}, the region dominated by the stretching vibrations due to O-H bonds. The integration was carried out using the following calibration (Paterson 1982):

$$C_{OH}=\frac{B_i}{150\zeta}\int\frac{H(\nu)}{(3780-\nu)} \quad (1)$$

where C_{OH} is the molar concentration of hydroxyl, ζ is an orientation factor, and $H(\nu)$ is the absorption coefficient in mm^{-1} at wavenumber ν in cm^{-1}. Based on published data for unit cell volumes, values for B_i of 4.39×10^4, 4.08×10^4 and 3.97×10^4 H/10^6Si were used for $i = \alpha$, β and γ, respectively. For spectra obtained in the (010) plane of the α phase, a value of $\zeta = 1/2$ was used for unpolarized radiation (Mackwell and Kohlstedt 1990); for spectra obtained from randomly oriented grains of the β and γ phases, a value of $\zeta = 1/3$ was used.

The calibration of extinction coefficients by Paterson (1982) used in the present study is based on an empirical correlation between OH-stretching frequency and extinction coefficient. However, it is possible that this correlation itself is matrix-dependent. The data reported in this paper on the concentration of water dissolved in olivine and its high-pressure polymorphs are, therefore, only first-order estimates, which might have to be recalculated once independent measurements of the extinction coefficients for OH in these phases are available. The accuracy of water contents reported in this paper is probably in the range 30 to 50%. Nonetheless, the ratios of water contents in different samples of the same phase are accurate to 1% or better.

Results

Microstructure and composition of hydrothermally annealed samples

Four features characterized samples hydrothermally annealed in the ***α***-stability field. First, the rectangular shape of the olivine crystals is well-preserved, as illustrated with the scanning electron micrograph in Fig. 1a. Second, all of the samples are fractured, most of them more severely than the one shown in Fig. 1a. Third, the exterior of the crystals reacted with the buffer powders, resulting in epitaxial overgrowths of olivine. The overgrowths visible in Fig. 1a are enriched in Mg and Ni but depleted in Fe relative to the starting sample; the material immediately in contact with the olivine crystal is nearly pure Fo_{100}, while the Mg:Ni ratios in the somewhat lighter grains with faceted faces is ~15:1. A thin region containing Ni and NiO separates the silicate material from the Pt jacket. Fourth, the interiors of samples contain a significant population of fluid inclusions Fig. 1b. The composition of the annealed samples is identical to that of the starting crystal, $(Mg_{0.90}Fe_{0.10}Ni_{0.003})_2SiO_4$.

The original shape of the olivine crystals can also be recognized in the samples hydrothermally annealed to produce the ***β*** phase, as illustrated in Fig. 2a. However, samples of the ***β*** phase are polycrystalline with a grain size of ~100 μm, Fig. 2b. While the Mg:Fe ratio of 9.60:1 in the ***β*** phase is similar to that in the starting sample (9.24:1) and the Ni content is essentially identical as well, the Me:Si (Me=Mg+Fe+Ni) ratio in the ***β*** grains is only 1.90:1 rather than 2.00:1 as in the starting crystal. In addition, the total oxide content in the ***β*** phase is only 97–98 wt%. The ***β*** phase is surrounded by a Mg-

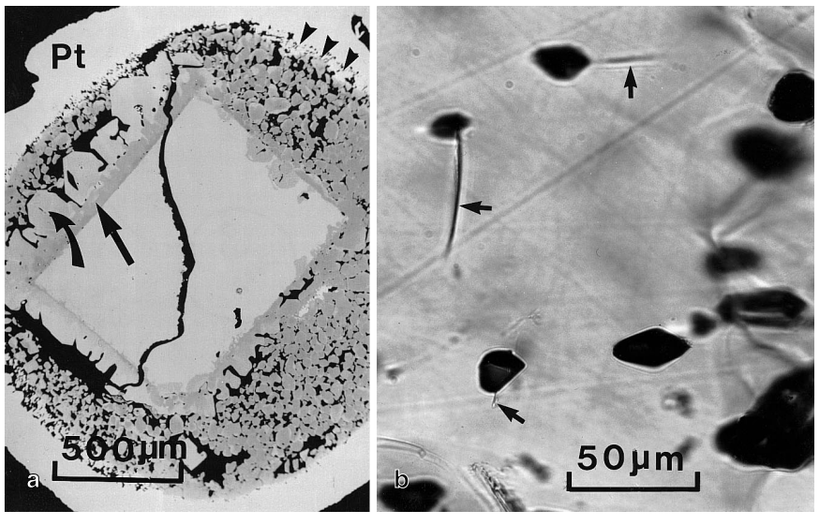

Fig. 1a Backscattered SEM image of sample ***α***1. A fracture cuts across the rectangular-shaped olivine crystal. Olivine rich in Mg (*straight arrow*) and olivine rich in Mg and Ni (*curved arrow*) surround the sample. A fine-grained mixture of olivine and enstatite, produced from the talc-brucite buffer powders, lies between the sample and the capsule. The entire assembly is enclosed in Pt, with a thin layer of Ni plus NiO (*arrow heads*) along the inner surface of the Pt. **b** Transmitted light image of fluid inclusions in sample ***α***2. Cracks (*arrows*) commonly emanate from the ends of the inclusions

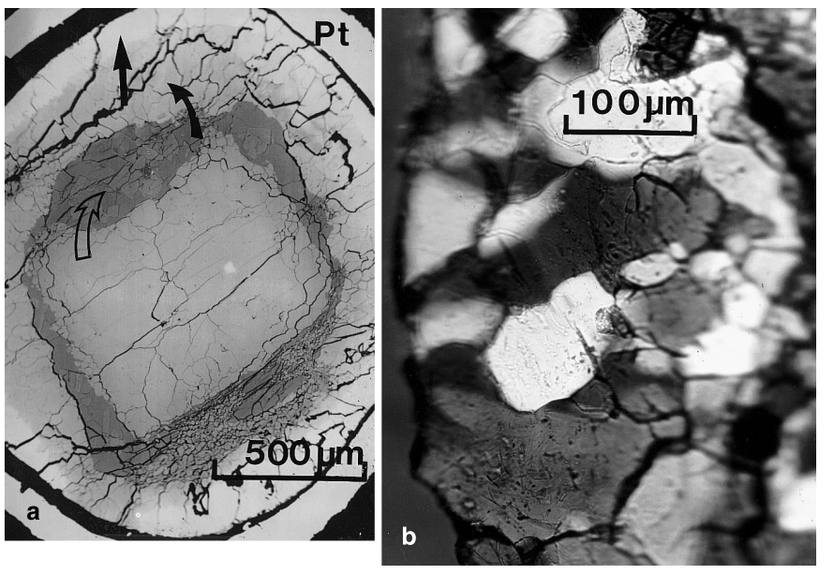

Fig. 2a Backscattered SEM image of sample ***β***3. The rectangular shape of the starting olivine crystal is clearly visible, surrounded by a Mg-rich, Fe-Ni-poor region (*open curved arrow*). This region is surrounded by a region with a similar Me:Si, but deplete in Fe (*solid curved arrow*). The region next to the Pt capsule also has olivine stoichiometry with a Mg:Ni ratio of ~1.5. **b** Transmitted light image of sample ***β***3 illustrating the polycrystalline nature of the samples of the ***β*** phase

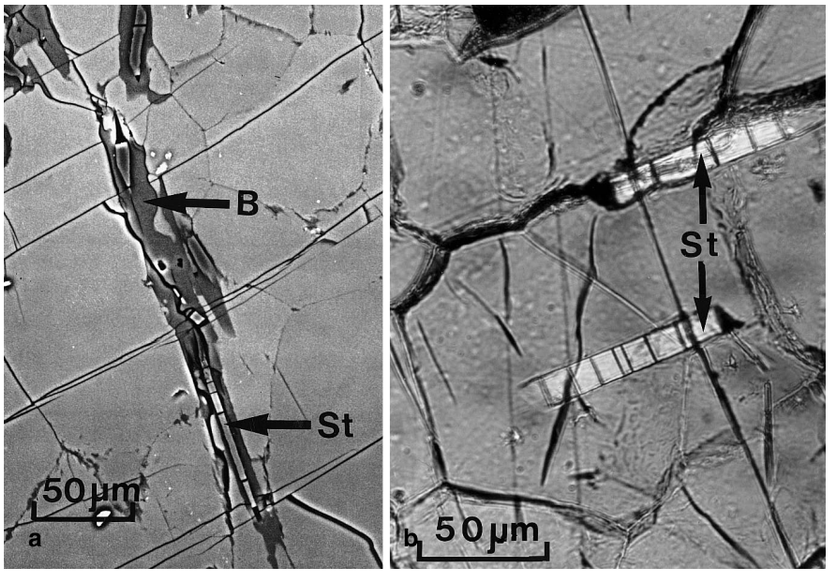

Fig. 3a Backscattered SEM image of sample $\gamma 2$. Long grains of stishovite (St) are separated from the γ-phase matrix by hydrous B phase. **b** Transmitted light image of bamboo-shaped grains of stishovite in sample $\gamma 2$; phase B, though present, is not visible

rich, Fe-Ni-poor region (the darker region in Fig. 2a) with approximately olivine stoichiometry. This region is in turn surrounded by a zone of material with a Me:Si ratio of ~1.90:1, with a Mg:Ni ratio of ~10:1 and very little Fe. The layer next to the Pt capsule also has olivine stoichiometry but with a Mg:Ni ratio of ~1.5:1 and almost no Fe. Particles of Ni and (Ni,Mg)O less than 10 µm across are present in this layer. The inner 10–20 µm of the capsule is a Pt-Ni alloy, with the Ni concentration decreasing with increasing distance from the sample charge. Based on X-ray diffraction analyses, the central, rectangular region in Fig. 2a is indeed β phase.

The water-rich sample of the γ phase ($\gamma 2$) is characterized by the presence of at least three phases, as illustrated in Fig. 3a. Grains of the phase approximately 100 µm across contain long, thin grains of a second phase that are surrounded by a more irregularly shaped areas of a third phase; a large region containing mostly the latter two phases phase is also present at one end of the sample. The Mg:Fe ratio in the γ phase is ~20:1, and the Me:Si ratio is ~1.95:1. As with the β phase, the total oxide content is low, in this case, 98–99 wt%; the Ni concentration is slightly lower than in the starting sample. The long, thin bamboo-shaped grains, Fig. 3b, are essentially free of Mg, Fe and Ni and have a Si:O ratio of ~1:2. The darker material noted in Fig. 3a has a Me:Si ratio of ~3:1 and a Mg:Fe ratio of ~60:1, with only a very small amount of Ni. X-ray diffraction indicates that these two phases are stishovite and the hydrous phase B, respectively, consistent with the measured compositions.

Hydroxyl solubility in the α phase

Eleven experiments were performed at 1100 °C and one at 1000 °C in the α-stability field at pressures between 2.5 and 13 GPa. Water was present in nine of the capsules at the completion of the experimental run. Table 1 summarizes the values for water solubility calculated from unpolarized infrared spectra of the resulting samples using Eq. (1).

Unpolarized FTIR spectra from samples hydrothermally annealed at 5, 8, 10 and 12 GPa are presented in Fig. 4. The infrared beam is strongly absorbed in the wavenumber range 3650 to 3450 cm^{-1}. A large absorption peak occurs near 3567 cm^{-1}, and three smaller peaks exist near 3613, 3598 and 3579 cm^{-1}. The peak at 3567 cm^{-1} increases systematically with increasing confining pressure (water fugacity), while the smaller peaks appear to saturate at an absorption coefficient of ~4 mm^{-1}.

The solubility data from the present study are compared with those of Bai and Kohlstedt (1992) in a log-log plot of C_{OH} versus f_{H_2O} in Fig. 5. Also included in this

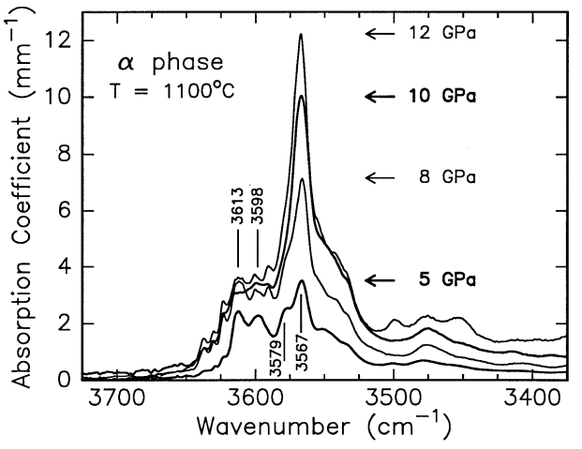

Fig. 4 Unpolarized FTIR spectra obtained on samples hydrothermally annealed at confining pressures of 5, 8, 10 and 12 GPa in the α-stability field at 1100 °C. The wavenumbers for four absorption peaks are labeled

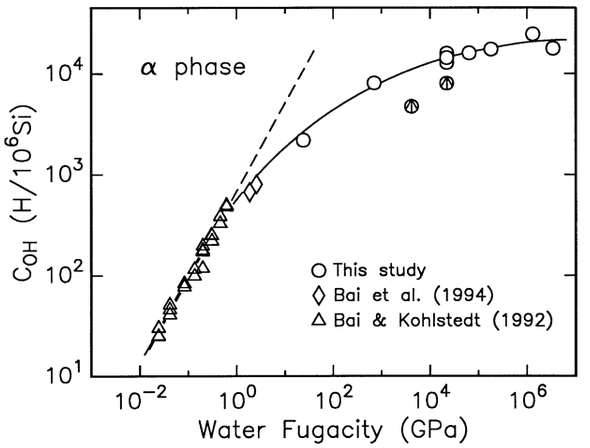

Fig. 5 Log-log plot of OH solubility versus water fugacity. *Circles* are data obtained in the present study; *circles containing arrows* denote runs in which no water was present at the end of the hydrothermal anneal. The data at 8 GPa have been separated along the vertical axis so that all three points are visible. *Triangles* are results from gas-medium experiments of Bai and Kohlstedt (1992), combined with more recent results from our laboratory. *Diamonds* are data from solid-medium experiments of Bai, Bai and Kohlstedt (1994, private communication). The *dashed line* is a linear least squares fit to the data of Bai and Kohlstedt (1992). The curved line is calculated from Eq. 16 with $A(T) = 1.1$ H/10^6Si at 1100 °C and $\Delta V_{\{\}} = 10.6\times10^{-6}$m^3/mol with the f_{H_2O} calculated from Pitzer and Sterner (1994), as described in the Discussion section

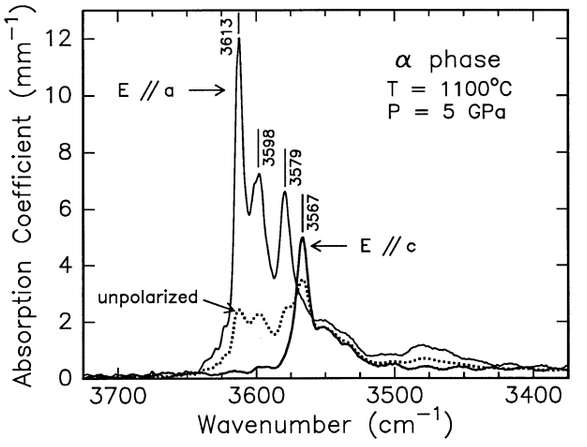

Fig. 6 Unpolarized and two polarized FTIR spectra obtained on a sample hydrothermally annealed in the ***α*** field at 5 GPa and 1100 °C. Four dominant absorption peaks are labeled

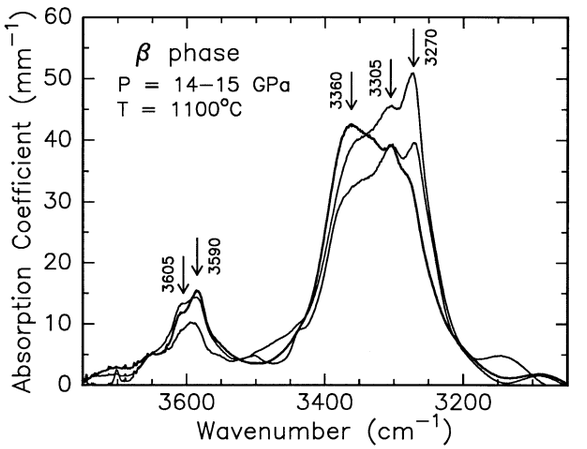

Fig. 7 Unpolarized FTIR spectra from three samples of ***β*** phase produced under hydrothermal conditions. The lower curve is from a sample prepared at 14 GPa, 1100 °C; the upper two curves are from samples synthesized at 15 GPa, 1100 °C. The sinusodial variation at wavenumbers below 3200 cm^{-1} are interference fringes. Two distinct groups of absorption bands are present. The wavenumbers of five absorption peaks are labeled

figure are two data points from experiments performed at 1.0 and 1.2 GPa (Bai, Bai and Kohlstedt, private communication, 1994) and nine data points from hydrothermal experiments at 0.4 and 0.5 GPa (Bai and Kohlstedt, private communication, 1994). To permit direct comparison with previous results, solubility data were obtained from unpolarized FTIR spectra using the calibration given in Eq. 1. Above ~1 GPa, the solubility results begin to deviate significantly from the power law relation (dashed line) between solubility and water fugacity reported by Bai and Kohlstedt (1992). At higher pressures, the data lie substantially below the values predicted by a linear extrapolation of the results obtained at lower pressures.

Polarized FTIR spectra with the electric field vector, *E*, parallel to either the *a* or the *c* crystallographic directions are compared with an unpolarized spectrum in Fig. 6. Three of the four prominent peaks in the unpolarized spectra are observed in the polarized spectrum with *E* parallel to *a*. Only the peak near = 3567 cm^{-1} appears in the polarized spectrum with *E* parallel to *c*. Hydroxyl concentration can also be calculated from the polarized spectra once a suitable calibration becomes available.

Hydroxyl solubility in the ***β*** phase

As illustrated in Fig. 7, a group of large absorption peaks near 3300 cm^{-1} and a second group of smaller peaks near 3600 cm^{-1} characterize unpolarized FTIR spectra from samples of the ***β*** phase prepared under hydrothermal conditions. Distinct peaks near 3360, 3305 and 3270 cm^{-1} comprise the first group. The second group includes peaks near 3605 and 3590 cm^{-1}. The OH content in the ***β*** phase is ~400,000 H/10^6Si.

The OH contents in the samples annealed at 15 GPa are about 10% higher than that in the sample annealed at 14 GPa. This difference may be due to sample-to-sample variations or may reflect the higher water fugacity in the higher-pressure experiments.

Hydroxyl solubility in the ***γ*** phase

Unpolarized FTIR spectra from one of the two samples of the ***γ*** phase (***γ***2) exhibit strong absorption in the wave-

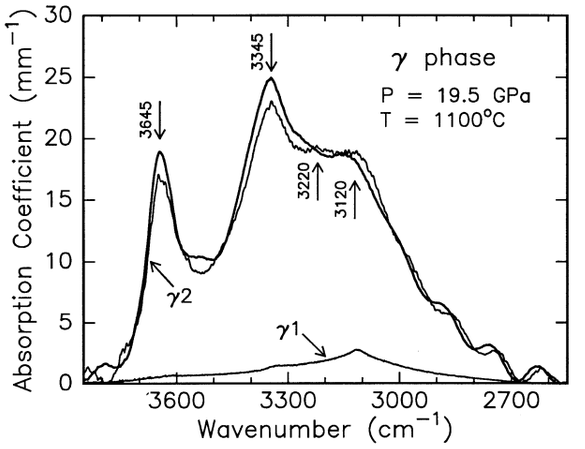

Fig. 8 Unpolarized FTIR spectra from two samples of the γ phase. The upper two spectra are from a sample synthesized from a single crystal of olivine; the sample was first held in the β field for one hour and then in the γ field for two hours. The lower spectrum is from a sample synthesized from olivine powders and annealed only in the γ-stability field. Four peaks have been labeled in the larger spectra; three of the four can be identified in the smaller spectra if it is enlarged

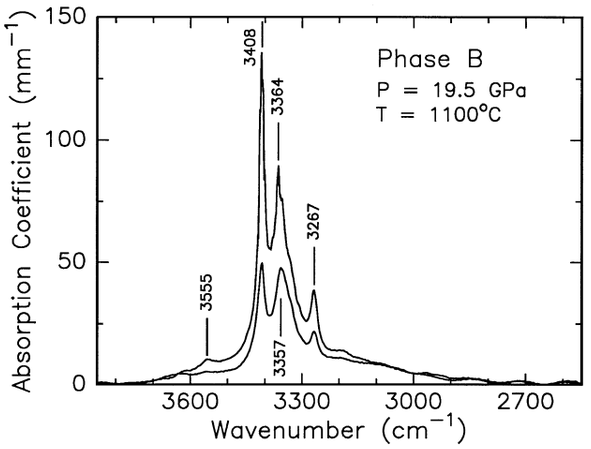

Fig. 9 Unpolarized FTIR spectra from two regions containing bamboo-shaped grains of stishovite surrounded by hydrous phase B in sample γ2. Four absorption peaks are identified by wavenumber

number range 3700 to 2700 cm^{-1}, as demonstrated in Fig. 8. This sample was synthesized from a crystal of olivine embedded in powders of talc plus brucite; the sample was held in the β field for one hour before increasing the pressure into the γ field. The peaks near 3645, 3345, 3220 and 3120 cm^{-1} dominate. As this sample was only 25 μm thick, sinusodial oscillations at wavenumbers between 2900 and 2600 cm^{-1} result from interference between light passing straight through the sample and light reflected from the two surfaces of the sample. The OH content in this sample is ~440,000 H/10^6Si.

The other sample of the γ phase (γ1) contains a substantially smaller amount of hydroxyl, ~32,000 H/10^6Si. This sample was prepared from olivine plus enstatite powders surrounded by talc plus brucite powders; the sample was annealed only in the γ field. The resulting grain size was ~10 μm. In Fig. 8, the three absorption peaks resolved in the FTIR spectrum from sample γ1 are at 3615, 3325 and 3115 cm^{-1}.

The FTIR spectra in Fig. 9 from regions within the γ phase containing grains of stishovite surrounded by hydrous phase B (see Fig. 3) exhibit strong absorption peaks near 3408, 3364, 3357 and 3267 cm^{-1}. The maximum peak height in the larger of the two spectra is approximately 10, 3 and 5 times higher than the peaks in spectra from the α, β and γ phases, respectively. Previously, investigators reported absorption peaks near 3410 and 3350 cm^{-1} from hydrous phase B (Akaogi and Akimoto 1986; Finger et al. 1989; McMillan et al. 1991). The peak near 3270 cm^{-1} may correspond to the weak absorption peak observed at 3240 cm^{-1} for stishovite synthesized at 10 GPa and 1200 °C (Pawley et al. 1993). However, the sharp absorption peak at 3111 cm^{-1} reported earlier in stishovite is absent, possibly due to compositional differences.

Discussion

FTIR spectra for the α phase

Unpolarized and polarized FTIR spectra from an olivine sample hydrothermally annealed at 5 GPa as part of the present study are compared in Fig. 10 with spectra from a sample hydrothermally annealed at 0.3 GPa by Bai and Kohlstedt (1992). Qualitatively the FTIR spectra from these two samples are similar, though quantitatively they differ in terms of the relative heights of various peaks. In the unpolarized spectra and the polarized spectra with E parallel to c, Figs. 10a and 10c, the peak near 3570 cm^{-1} dominates. This peak also dominates for the sample annealed at 0.3 GPa in the polarized spectrum with E parallel to a, Fig. 10b. However, the peak at 3613 cm^{-1} is larger for the sample annealed at 5 GPa with E parallel to a. The peak near 3525 cm^{-1} in all three spectra from the sample annealed at the lower pressure is absent in the spectra from the sample annealed at the higher pressure.

The observations reported above are largely consistent with those made based on infrared spectra of naturally occurring olivine (Beran and Putnis 1983; Miller et al. 1987). One exception is the relatively large peak at 3567 cm^{-1} in the spectrum with E parallel to c from the sample annealed at 5 GPa; this peak is absent in the spectrum with E parallel to a. In previous studies, the heights of peaks near this wavenumber are either similar in the two polarized spectra or larger in spectra with E parallel to a. The exact roles of pressure and composition on such peaks are not yet clear. A major difference between spectra from natural olivine crystals (e.g., Miller et al. 1987) and spectra from crystals hydrothermally annealed as part of the present study is the fact that the natural sam-

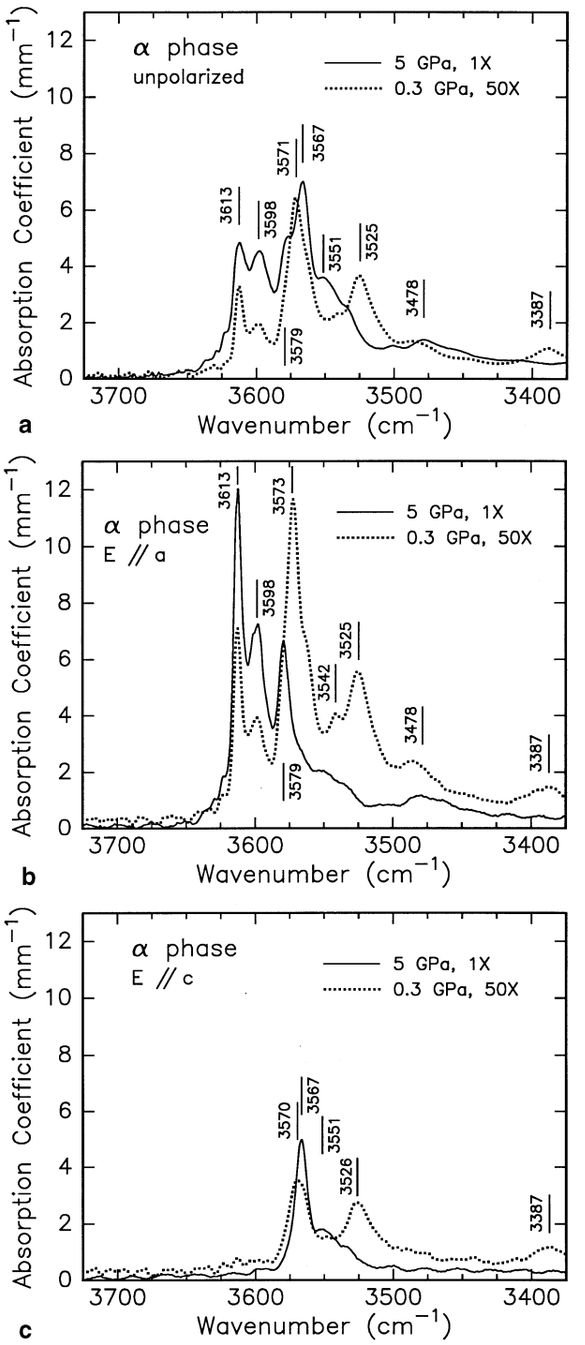

Fig. 10a–c Comparison of FTIR spectra for an olivine crystal hydrothermally annealed at 5 GPa with one annealed at 0.3 GPa; **a** unpolarized spectra, **b** spectra with *E // a* and **c** spectra with *E // c*. The sample hydrothermally annealed at 5 GPa is from the present study; the sample annealed at 0.3 GPa is from Bai and Kohlstedt (1993) and was heat-treated at 1300°C. The spectra from the 0.3-GPa sample have been enhanced by a factor of 50 to facilitate the comparison

ples often contain a much larger number of distinct absorption bands, probably due to chemical impurities.

Hydroxyl as a point defect in olivine

A number of possible sites have been proposed for the incorporation of hydroxyl in the olivine structure (Beran 1969; Beran and Putnis 1983; Mackwell and Kohlstedt 1990; Bai and Kohlstedt 1992, 1993; Wright and Catlow 1994). Two of these possibilities are discussed below in the context of the present experimental results.

Based on the results of atomistic simulation calculations, Wright and Catlow (1994) obtained a relatively low energy of solution if OH is incorporated via a reaction between olivine and water in which ferric iron is reduced to ferrous iron:

$$2Fe^{\bullet}_{Me} + 2O^{x}_{O} + H_2O\ (fl) \rightarrow 2Fe^{x}_{Me} + 2(OH)^{\bullet}_{O} + \frac{1}{2}O_2\ (fl) \quad (2)$$

where the Kröger-Vink defect notation has been used to specify species, site and charge of defects in the olivine structure (Kröger and Vink 1956) and the notation (*fl*) indicates a component in the (hydrous) fluid phase. If reaction 2 is combined with the reaction

$$\frac{1}{2}O_2\ (fl) + 3Fe^{x}_{Me} \rightarrow V''_{Me} + 2Fe^{\bullet}_{Me} + FeO\ (fl) \quad (3)$$

the associated mass action equation yields

$$[V''_{Me}]\,[(OH)^{\bullet}_{O}]^2 \propto f^{1}_{H_2O}. \quad (4)$$

As the concentration OH increases, the reduction of ferric iron to ferrous iron in reaction 3 suggests that the charge neutrality condition $[Fe^{\bullet}_{Me}] = 2[V''_{Me}]$, which is applied to olivine buffered by orthopyroxene under anhydrous conditions, should be replaced by

$$[(OH)^{\bullet}_{O}] = 2[V''_{Me}]. \quad (5)$$

The observation that physical properties such as high-temperature creep strength are dramatically affected by the presence of water (e.g., Chopra and Paterson 1984; Mackwell et al. 1985; Karato et al. 1986) indeed indicates that the introduction of OH into the olivine structure affects the charge neutrality condition. Equations (3) and (5) can now be combined to obtain the dependence of hydroxyl content on water fugacity:

$$[(OH)^{\bullet}_{O}] \propto f^{1/3}_{H_2O}. \quad (6)$$

From Eqs. 3 and 6, the dependence on water fugacity of the concentrations of defect complexes of the type $(OH)^{\bullet}_{O} + V''_{Me} \rightarrow \{(OH)^{\bullet}_{O} - V''_{Me}\}^{\cdot}$ and $2(OH)^{\bullet}_{O} + V''_{Me} \rightarrow \{2(OH)^{\bullet}_{O} - V''_{Me}\}^{x}$ will then be

$$[\{(OH)^{\bullet}_{O} - V''_{Me}\}^{\cdot}] \propto f^{2/3}_{H_2O} \quad (7)$$

and

$$[\{2(OH)^{\bullet}_{O} - V''_{Me}\}^{x}] \propto f^{1}_{H_2O} \quad (8)$$

Based on measurements of the solubility of hydroxyl in olivine as a function of water fugacity, it has been suggested that the interstitial defect $(OH)_I'$ may also be an important site for the incorporation of hydroxyl into the olivine structure (Bai and Kohlstedt 1992, 1993). This defect can be incorporated into the olivine structure through the reaction

$$O_O^x + H_2O + V_I^x \rightarrow (OH)_O^{\cdot} + (OH)_I'. \quad (9)$$

In this case, the charge neutrality condition might be expected to involve the two defects on the right-hand side of reaction (9), that is,

$$[(OH)_O^{\cdot}] = [(OH)_I']. \quad (10)$$

If the law of mass action for Eq. 9 is combined with Eq. 10, the dependencies of the concentrations of these defects on water fugacity will be

$$[(OH)_O^{\cdot}] = [(OH)_I'] \propto f_{H_2O}^{1/2}. \quad (11)$$

Based on Eq. 11 the concentration of defect complexes formed by the reaction $(OH)_O^{\cdot} + (OH)_I' \rightarrow \{(OH)_O^{\cdot} + (OH)_I'\}^x$ will have the following dependence on water fugacity:

$$[\{(OH)_O^{\cdot} - (OH)_I'\}^x] \propto f_{H_2O}^{1}. \quad (12)$$

The primary experimental constraint on the speciation of water-derived defects in olivine comes from an investigation of the solubility of hydroxyl as a function of water fugacity (Bai and Kohlstedt 1992). In a series of hydrothermal annealing experiments on olivine single crystals at pressures between 50 and 300 MPa (water fugacities between 25 and 315 MPa), these authors observed a systematic increase in OH concentration with increasing water fugacity. If their Group I and their Group II FTIR bands are combined, then

$$C_{OH} \propto f_{H_2O}^{0.9}. \quad (13)$$

Based on the types of incorporation mechanisms discussed above, a water fugacity exponent greater than 0.5 indicates that a significant fraction of the hydroxyl must be associated with other charged defects, such as those considered in Eqs. 7, 8 and 12, as no evidence exists in the IR spectra that would suggest that a significant amount of molecular water is present. In the optically clear and inclusion-free regions of the samples studied by micro-FTIR spectroscopy, neither the H_2O bending vibration at 1630 cm^{-1} nor the combination band of molecular water at 5200 cm^{-1} were ever observed. Because of the strong absorbance in the OH stretching region, these bands should be resolved if a significant fraction of the total water were present in molecular form.

Thermodynamics of water in olivine

To interpret the solubility results reported in the present paper, the effect of both pressure and water fugacity must be taken into account. In the present analysis, it is assumed that most of the hydroxyl forms defect associates, consistent with the high value (>0.5) of the water fugacity exponent (Bai and Kohlstedt 1992) and with the very high concentrations of hydroxyl introduced into olivine in the high-pressure hydrothermal anneals. In particular, it is assumed that most of the OH is incorporated through reaction 9, but note that the conclusions reached in the following analysis are not dependent on this assumption.

The mass action equation for the introduction of OH via reaction 9 combined with the formation reaction for the defect complex $\{(OH)_O^{\cdot} - (OH)_I'\}^x$ yields the equilibrium constant, K,

$$K(T,P,f_{H_2O}) = \exp\left(\frac{-\Delta G_{\{\}}}{RT}\right) = \frac{[\{(OH)_O^{\cdot} - (OH)_I'\}^x]}{[O_O^x]\ f_{H_2O}[V_I^x]} \approx \frac{[\{(OH)_O^{\cdot} - (OH)_I'\}^x]}{f_{H_2O}} \quad (14)$$

where $\Delta G_{\{\}}$ is the Gibbs energy associated with replacing an oxygen ion and a vacant interstitial site with OH^- ions and forming a defect complex; RT has its usual meaning. Therefore, the dependence of OH concentration on pressure and water fugacity is given by the equation

$$[\{(OH)_I^{\cdot} - (OH)_I'\}^x] = f_{H_2O} \exp\left(-\frac{P\Delta V_{\{\}}}{RT}\right) \exp\left(-\frac{\Delta H_{\{\}} - T\Delta S_{\{\}}}{RT}\right) \quad (15)$$

where P is pressure, $\Delta V_{\{\}}$, $\Delta H_{\{\}}$ and $\Delta S_{\{\}}$ are the changes in molar volume, enthalpy and entropy due to the incorporation of OH into olivine.

Dependence of hydroxyl solubility on pressure for olivine

The dependence of hydroxyl solubility on pressure is governed by the term $P\Delta V_{\{\}}$ in Eq. 15. To determine the magnitude of $\Delta V_{\{\}}$, Eq. 15 is rewritten in the form

$$C_{OH}(T,P,f_{H_2O}) = A(T)\ f_{H_2O}^n \exp(-P\Delta V_{\{\}}/RT) \quad (16)$$

and the solubility data are presented as a semi-log plot of C_{OH}/f_{H_2O} versus P in Fig. 11. If a water fugacity exponent of unity is used, as suggested by Eq. 12, this analysis yields $A(T)$ = 1.1 H/10^6Si at 1100 °C and $\Delta V_{\{\}}$ = 10.6×10^{-6} m^3/mol. If a water fugacity exponent of 0.9 is used, as given by Eq. 13 (Bai and Kohlstedt 1992), the molar volume term decreases to $\Delta V_{\{\}} = 8.5\times0^{-6}$ m^3/mol.

Hydroxyl solubility in the β phase

In an experiment at 14.5 GPa and 850 °C, McMillan et al. (1991) synthesized a sample of β-Mg_2SiO_4 with ~9000 H/10^6Si. Subsequently, in a run at 14 GPa and 1275 °–1375 °C, Young et al. (1993) produced a sample of β-$(Mg,Fe)_2SiO_4$ with a substantially larger OH con-

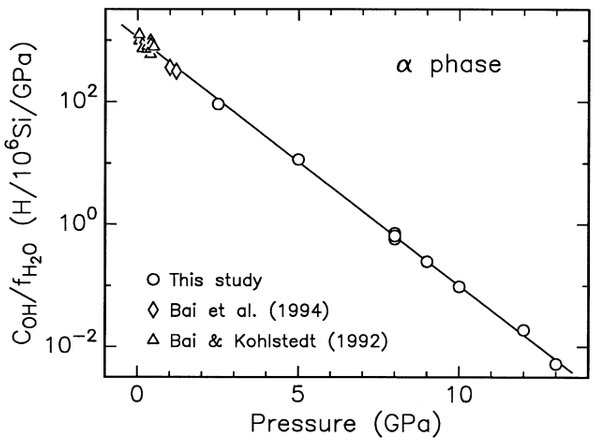

Fig. 11 Semi-log plot of OH concentration divided by water fugacity versus confining pressure for samples annealed in the ***α***-stability field. The molar volume change resulting from the incorporation of hydroxyl into the olivine structure is calculated from the slope of the linear least-squares fit of these data, as illustrated in Eqs. 15 and 16. The three data points at 8 GPa have been separated for clarity; the low-pressure data are plotted so as not to overlie one another. See the caption for Fig. 5 for additional information

tent, ~65,000 H/10^6Si. In neither case was water intentionally included in the sample capsule. As a result, the concentrations of OH in their samples are substantially smaller than in ours, $C_{OH} \approx$ 400,000 H/10^6Si. As in the two previous studies, the infrared spectra in Fig. 7 contain strong absorption peaks near $\nu \approx 3300$ cm^{-1} and weaker peaks at 3600 cm^{-1}.

Two models exist for the possible sites for the incorporation of OH and the resulting crystallographic structure of the ***β*** phase. Smyth (1987) suggested that the O(1) structural site is the most likely oxygen position for protonation, while Downs (1989) favored the O(2) as well as the O(1) site. Based on ionic constraints and subgroup symmetry, Smyth (1994) proposed a maximum OH content of 500,000 H/10^6Si (33,000 wt ppm) and a composition of $Mg_7Si_4O_{14}(OH)_2$ for fully hydrated ***β*** phase. Substitution of two hydrogens for one M(2) magnesium (i.e., Eq. 5) maintains charge neutrality, or in point defect notation,

$$V''_{Mg} + 7Mg^x_{Mg} + 4Si^x_{Si} + 14O^x_O + 2(OH)^{\cdot}_O. \quad (17)$$

Cynn and Hofmeister (1994) argued that the infrared absorption peak near 3330 cm^{-1} is associated with protonation of the O(2) site and the absorption bands near 3600 cm^{-1} are due to protonation of the O(1) site. Based on this assignment of absorption peaks to protonation of specific oxygen sites, over two-thirds of the hydrogen in our samples is bonded to O(2).

The Me:Si ratio of 1.90:1 measured for our samples is larger (i.e., the metal vacancy concentration is smaller) than the predicted value of 1.75:1 (i.e., $[V''_{Me}] = 0.125$) for OH-rich ***β*** phase. However, the OH content of 400,000 H/10^6Si in our samples is larger than the value of 200,000 H/10^6Si expected based on expression 17 for Me:Si = 1.90. One possible explanation for this difference is related to the presence of Fe in our samples. Iron can affect charge neutrality and, therefore, OH solubility if some fraction is present as ferric iron in silicon sites, Fe'_{Si}. In this case, positively charged $(OH)^{\cdot}_O$ defects would be charge compensated by two negatively charged point defects, V''_{Me} and Fe'_{Si}. This interpretation is supported by the results recently reported by Inoue (1994) for solubility of water in the ***β*** phase. In experiments on Fe-free samples at 15.5 GPa and 1200 °C, water concentrations of about 450,000 H/10^6Si and Mg:Si ratios of about 1.78:1 were reported. These values are close to those proposed by Smyth (1994) for the Mg end member of the ***β*** phase. Alternatively, the discrepency between water content and Me:Si ratio may be due to the inaccuracy in the OH content calculated using Eq. (1).

Hydroxyl solubility in the ***γ*** phase

The hydroxyl concentration in the ***γ*** phase hydrothermally annealed at 19.5 GPa and 1100 °C, ~450,000 H/10^6Si, is similar to that determined for the ***β*** phase at 14–15 GPa and 1100 °C, ~400,000 H/10^6Si. The Me:Si ratio in the ***γ*** phase, however, is somewhat larger, 1.95:1, than in the ***β*** phase, 1.90:1. Absorption peaks due to OH-stretching vibrations from the region containing stishovite and hydrous phase B, Fig. 9, are absent in FTIR spectra from the ***γ*** phase, Fig. 8. These observations indicate that the high OH concentrations determined here for the ***γ*** phase are not due to a fine intergrowth of a hydrous phase with the ***γ*** phase.

The discrepancy in water content between the two samples prepared in the ***γ***-stability field is significant. As described in the section on Experimental Procedure, both the sample charge and the temperature-pressure path differed for the two samples. Because the absorption peaks occur at the same wavenumbers for the two samples, the lower water content in sample ***γ***1 is probably due to escape of water from the capsule rather than differences in the hydrothermal annealing procedure. Additional experiments are needed to explore this point.

Geochemical implications

Our data demonstrate that the equilibrium solubility of water in olivine is much higher than expected from measurements on natural samples from a variety of tectonic settings (e.g., Beran and Putnis 1983; Miller et al. 1987; Bell and Rossman 1992) or experimental samples annealed previously near the ***α*-*β*** phase boundary (Young et al. 1993). Between 5 and 10 GPa, 500–1000 ppm by weight of H_2O can be incorporated in the olivine structure. Therefore, the total water content of the upper mantle could be incorporated in this mineral alone. Bell and Rossman (1992) argue that the solubility in pyroxenes should be even higher, and some of our preliminary experiments (to be published elsewhere) support this

conclusion. Consequently, under normal conditions, a free hydrous fluid phase will not be stable in the upper mantle except in special tectonic environments such as the mantle wedge above a subducting slab. Similarly, special hydrous phases are not needed for storing water in the mantle.

The high equilibrium solubility of water in olivine has important consequences for processes occurring in subduction zones. The generation of magmas in subduction zones occurs when hydrous fluids released from the subducting slab infiltrate the mantle wedge and the temperature exceeds the water saturated solidus. In principle, an accurate thermal model of the subduction zone should be able to predict precisely where magma generation occurs. This situation will no longer hold true if the released fluid interacts with nominally anhydrous minerals. Because these minerals can store enormous amounts of water, the presence of a free fluid phase and, therefore, the onset of melting will depend on the relative rates of water release from the subducted slab and water incorporation in olivine and pyroxene. A static picture of the thermal structure of a subduction zone, even if it is perfectly accurate, will not be able to predict where melting occurs. Furthermore, interaction of a subduction zone fluid with anhydrous minerals will change the composition of the fluid. Upon release from the slab, the fluid will contain significant amounts of halogens, particularly chlorine, since it originates from material that had been in contact with sea water. Although the original chloride content of the fluid might be small, it will become more and more concentrated as water is absorbed by anhydrous minerals while the fluid is percolating through the mantle wedge. The fluid causing metasomatism of the source region of magmas in subduction zones might therefore be a highly concentrated salt brine rather than a dilute aqueous solution.

The very high solubility of water in the β phase has led some scientists to suggest that water should be strongly enriched in the transition zone (e.g., Smyth 1987; Young et al. 1993). This conclusion is very likely to be true; however, the precise concentration of water in the transition zone is difficult to estimate. Extrapolation of our thermodynamic model for the solubility of water in olivine into the β-stability field yields a partition coefficient for water between the β and α phases of $D^{\beta/\alpha} = 20$. This value is in fact a minimum for the partition coefficient, because the lack of water at the end of the experiments on the β phase suggests that these samples may have been undersaturated; in contrast, the presence of water following most of the hydrothermal anneals on olivine suggests that they were saturated (Table 1). This result is consistent with that of Young et al. (1993) who determined a value for $D^{\beta/\alpha}$ of 40 from samples containing grains of both α and β. However, none of their experiments were conducted in the presence of excess water, and therefore their measured water contents are much lower than those given in this paper. The problem in evaluating the water content of the transition zone, assuming it is in chemical equilibrium with the upper mantle, is the unknown solubility of water in the pyroxenes. It appears that pyroxenes concentrate water relative to olivine (Bell and Rossman 1992; our own unpublished results), but the effect cannot yet be quantified. Any estimate of water partitioning between upper mantle and transition zone obviously must take the pyroxenes into account, which at present is not possible. One can only guess, therefore, that the transition zone is probably enriched in water, however, the effect cannot yet be quantified.

Based on the strong preference of water for the β phase and a seismologically constrained width for the transition zone of less than 10 km, Wood (1995) recently calculated the maximum concentration of water in olivine near the 410-km discontinuity. His analysis yields an upper limit of about 3400 H/10^6Si using $D^{\beta/\alpha} = 10$. Thus, combined with the values for solubility presented in Table 1 and Figs. 5 and 11 and the somewhat larger values for $D^{\beta/\alpha}$ discussed above, this result indicates that, away from regions of partial melting, the upper mantle is roughly 10–20% saturated with respect to water content.

Our observations of high water solubility in the phase together with some recent data for stishovite and perovskite (Pawley et al. 1993; Lu et al. 1994; Meade et al. 1994) make it very likely that the entire mantle has the capacity to store more than the water content of the total hydrosphere. Consequently, a hydrous fluid phase was not necessarily present in the mantle even before the hydrosphere formed by magmatic out-gassing. To test this and similar assumptions, however, quantitative thermodynamic models of the solubility of water in all major mantle minerals are needed, such as that presented here for olivine, based on experiments performed under well-controlled thermodynamic conditions.

Geophysical implications

Although water weakening is pronounced for both polycrystalline aggregates and single crystals of olivine (Carter and Ave'Lallemant 1970; Blacic 1972; Chopra and Paterson 1984; Mackwell et al. 1985; Karato et al. 1986), the dependence of creep rate on water fugacity or OH concentration remains undetermined. Two observations suggest that creep rate may increase approximately linearly with OH solubility. First, a recent analysis by Kohlstedt et al. (1995) of the creep data of Kronenberg and Tullis (1984) for quartz aggregates yields a nearly linear dependence of creep rate on water fugacity. Second, a comparison of creep data for olivine aggregates deformed at a confining pressure of 0.3 GPa (Karato et al. 1986) to data from creep experiments at 1.5 GPa (Borch and Green 1989) reveals that the samples deformed at the higher pressure were weaker than those deformed at the lower pressure. This result is opposite to that expected for the effect of pressure on creep rate through an activation volume term (e.g., Weertman and Weertman 1975) but consistent with a pronounced water-weakening effect. The magnitude of the discrepancy between the two sets of data suggests that creep rate is

approximately linearly dependent on water fugacity, that is, approximately linearly dependent on OH concentration, provided that the activation volume for creep is not too large (Kohlstedt et al. 1995). Thus, for a fixed oxygen fugacity and differential stress, the effect of increasing water solubility with increasing pressure (Fig. 7) is to increase creep rate by a factor of $\sim$10 as depth increases from 50 km to 400 km. This increase in strain rate will offset, at least to some degree, the decrease associated with the activation volume.

The presence of water should also markedly enhance the electrical conductivity of olivine. Two mechanisms can contribute. First, a highly mobile water-derived ion such as H^+ would directly enhance electrical conductivity in the mantle (Karato 1990). Second, the introduction of water-derived point defects will affect the concentrations of other point defects such as magnesium vacancies and, therefore, indirectly enhance electrical conductivity (Bai and Kohlstedt 1992, 1993). In a recent paper, Lizarralde et al. (1995) argued that results from a long-period magnetotelluric investigation of the electrical structure beneath the eastern North Pacific may indicate a significant contribution from H^+ ions. They observed electrical conductivities one to two orders of magnitude higher than those expected for dry olivine over the depth range 100 to 400 km, and demonstrated that this discrepancy is consistent with the results on water solubility as a function of pressure reported in Table 1, combined with published diffusivities for water-derived species in olivine (Mackwell and Kohlstedt 1990).

It has recently been argued that water should also have a pronounced effect on seismic wave velocity and attenuation (Karato 1995). Water increases the mobility of both point defects and dislocations in olivine and, thus, enhances anelastic relaxation processes with a resultant reduction in seismic velocity. The present results provide the basis, then, necessary for beginning to quantify the influence of water on the physical properties of nominally anhydrous minerals and, thus, the Earth's mantle.

Acknowledgements The Alexander von Humboldt Foundation and the National Science Foundation kindly funded this research through a Senior Scientist Research Award and grant EAR-9405470, respectively, to David Kohlstedt. Hubert Schulze, Detlef Krauße and Herbert Kufner furnished the technical assistance that made this research possible. Mike Sterner contributed substantially with calculations of water fugacity as a function of pressure and temperature. Susan Ginsberg provided critical comments that resulted in significant improvements in this document. Anne Hofmeister and Gregory Miller prepared helpful reviews. Shun Karato, Paul McMillan and Tatsuhiko Kawamoto made valuable comments. Fritz Seifert established the stimulating research environment that brought the authors together.

References

Akaogi M, Akimoto S (1986) Infrared spectra of high-pressure hydrous silicates in the system MgO-SiO_2-H_2O. Phys Chem Mineral 13: 161–164

Bai Q, Kohlstedt DL (1992) Substantial hydrogen solubility in olivine and implications for water storage in the mantle. Nature 357: 672–674

Bai Q, Kohlstedt DL (1993) Effects of chemical environment on the solubility and incorporation mechanism for hydrogen in olivine. Phys Chem Mineral 19: 460–471

Bell DR, Rossman GR (1992) Water in the earth's mantle: the role of nominally anhydrous minerals. Science 255: 1391–1397

Beran A (1969) Über (OH)-Gruppen in Olivin. Anz Österr Akad Wiss Math Naturwiss Kl Anzeiger 73–74

Beran A, Putnis A (1983) A model of the OH positions in olivine, derived from infrared-spectroscopic investigations. Phys Chem Mineral 9: 57–60

Blacic JD (1972) Effect of water on the experimental deformation of olivine. Geophys Monogr. Am Geophys Union 16: 109–115

Borch RS, Green HW II (1989) Deformation of peridotite at high pressure in a new molten salt cell: comparison of traditional and homologous temperature treatments. Phys Earth Planet Inter 55: 269–276

Canil D (1994) Stability of clinopyroxene at pressure-temperature conditions of the transition zone. Phys Earth Planet Inter 86: 25–34

Carter NL, Ave'Lallemant HG (1970) High temperature flow of dunite and peridotite. Geol Soc Am Bull 81: 2181–2202

Chopra PN, Paterson MS (1984) The role of water in the deformation of dunite. J Geophys Res 89: 7861–7876

Cynn H, Hofmeister AM (1994) High-pressure IR spectra of lattice modes and OH vibrations in Fe-bearing wadsleyite. J Geophys Res 99: 17,717–17,727

Downs JW (1989) Possible sites for protonation in β-Mg_2SiO_4 from an experimentally derived electrostatic potential. Am Mineral 74: 1124–1129

Finger LW, Ko H, Hazen RM, Gasparik T, Hemley RJ, Prewitt CT, Weidner DJ (1989) Crystal chemistry of phase B and a new anhydrous magnesium silicate: implications for water storage in the upper mantle. Nature 341: 140–142

Inoue T (1994) Effect of water on melting phase relations and melt composition in the system Mg_2SiO_4-$MgSiO_3$-H_2O up to 15 GPa. Phys Earth Planet Inter 85: 237–263

Karato S (1990) The role of hydrogen in the electrical conductivity of the upper mantle. Nature 347: 272–273

Karato S-I (1995) The effects of water on seismic wave velocities in the upper mantle. Proc Japan Acad 71: 61–66

Karato S-I, Paterson MS, FitzGerald JD (1986) Rheology of synthetic olivine aggregates: Influence of grain size and water. J Geophys Res 91: 8151–8176

Kohlstedt DL, Evans B, Mackwell SJ (1995) Strength of the lithosphere: constraints imposed by laboratory experiments. J Geophys Res 100: 17587–17602

Kröger FA, Vink HJ (1956) Relation between the concentration of imperfections in crystalline solids. In: F Seitz, D Turnhall (eds) Solid state physics 3. by Academic Press, New York, pp 367–435

Kronenberg AK, Tullis J (1984) Flow strengths of quartz aggregates: grain size and pressure effects due to hydrolytic weakening. J Geophys Res 89: 4281–4297

Lizarralde D, Chave A, Hirth G, Schultz A (1995) Long-period magnetotelluric study using Hawaii-to-California submarine cable data: implications for mantle conductivity. J Geophys Res 100: 17837–17854

Lu R, Hofmeister AM, Wang Y (1994) Thermodynamic properties of ferromagnesium silicate perovskites from vibrational spectroscopy. J Geophys Res 99: 11795–11804

Mackwell SJ, Kohlstedt DL (1990) Diffusion of hydrogen in olivine: implications for water in the mantle. J Geophys Res 95: 5079–5088

Mackwell SJ, Kohlstedt DL, Paterson MS (1985) The role of water in the deformation of olivine single crystals. J Geophys Res 90: 11319–11333

McMillan PF, Akaogi M, Sato RK, Poe B, Foley J (1991) Hydroxyl groups in β-Mg_2SiO_4. Am Mineral 76: 354–360

Meade C, Reffner JA, Ito E (1994) Synchrotron infrared absorbance measurements of hydrogen in $MgSiO_3$. Science 264: 1558–1560

Miller GH, Rossman GR, Harlow GE (1987) The natural occurrence of hydroxide in olivine. Phys Chem Mineral 14: 461–472

Paterson MS (1982) The determination of hydroxyl by infrared absorption in quartz, silicate glasses and similar materials. Bull Minéral 105: 20–29

Pawley AR, McMillan PF, Holloway JR (1993) Hydrogen in stishovite, with implications for mantle water content. Science 261: 1024–1026

Pitzer KS, Sterner SM (1994) Eqn.s of state valid continuously from zero to extreme pressures for H_2O and CO_2. J Chem Phys 101: 3111–3116DC,

Rubie DC, Karato S, Yan H, O′Neill HStC (1993a) Low differential stress and controlled chemical environment in multianvil high-pressure experiments. Phys Chem Mineral 20: 315–322

Rubie DC, Ross II CR, Carroll MR, Elphick, SC (1993b) Oxygen self-diffusion in $Na_2Si_4O_9$ liquid up to 10 GPa and estimation of high-pressure melt viscosities. Am Mineral 78: 574–582

Smyth JR (1987) β-Mg_2SiO_4: a potential host for water in the mantle? Am Mineral 72: 1051–1055

Smyth JR (1994) A crystallographic model for hydrous wadsleyite (β-Mg_2SiO_4): an ocean in the earth′s interior? Am Mineral 79: 1021–1024

Weertman J, Weertman JR (1975) High temperature creep of rock and mantle viscosity. Ann Rev Earth Planet Sci 3: 293–315

Wood BJ (1995) The effect of H_20 on the 410-kilometer seismic discontinuity. Science 268: 74–76

Wright K, Catlow CRA (1994) A computer simulation study of (OH) defects in olivine. Phys Chem Mineral 20: 515–518

Young TE, Green HW II, Hofmeister AM, Walker D (1993) Infrared spectroscopic investigation of hydroxyl in β-$(Mg,Fe)_2SiO_4$ and coexisting olivine: implications for mantle evolution and dynamics. Phys Chem Mineral 19: 409–422